Nanoscale

COMMUNICATION

View Article Online
View Journal | View Issue

Cite this: *Nanoscale*, 2018, **10**, 15164

Received 15th April 2018,
Accepted 21st July 2018

DOI: 10.1039/c8nr03058h

rsc.li/nanoscale

Significantly improved black phase stability of $FAPbI_3$ nanowires *via* spatially confined vapor phase growth in nanoporous templates†

Leilei Gu,‡[a] Daquan Zhang,‡[a] Matthew Kam,[a] Qianpeng Zhang,[a] Swapnadeep Poddar,[a] Yu Fu,[a] Xiaoliang Mo[b] and Zhiyong Fan *[a]

The formamidinium lead iodide ($FAPbI_3$) perovskite has attracted immense research interest as it has much improved stability than methylammonium lead iodide ($MAPbI_3$) while still maintaining excellent optoelectronic properties. Compared to $MAPbI_3$, $FAPbI_3$ has shown an elevated decomposition temperature and a slower decomposition process and therefore it is considered as a more promising candidate for future high-efficiency and reliable optoelectronic devices. However, these excellent optoelectronic properties only exist in the alpha phase and this phase will spontaneously transform into an undesired delta phase with much poorer optoelectronic properties regardless of the environment. This is the main challenge for the application of the $FAPbI_3$ perovskite. Herein, we report a novel strategy to stabilize the cubic black phase of $FAPbI_3$ by using nanoengineering templates. Without further treatment, the black phase can be held over 7 months under ambient conditions and 8 days in an extreme environment with a Relative Humidity (RH) of 97%. A systematic study further reveals that this great improvement can be attributed to the spatial confinement in anodized alumina membrane (AAM) nanochannels, which prohibits the unwanted α-to-δ phase transition by restricting the expansion of NWs in the *ab* plane, and the excellent passivation against water molecule invasion. Meanwhile, we also demonstrate the potency of these NWs in practical applications by configuring them into photodetectors, which have shown reasonable response and excellent device stability.

Introduction

The past few years have witnessed tremendous advancement of research on organometallic perovskite materials, which have emerged as the most compelling candidates for next-generation optoelectronic devices such as solar cells,[1–3] lasers,[4,5] light emitting diodes (LEDs),[6,7] photodetectors[8,9] *etc*. Among the family of organometallic perovskites, methylammonium lead iodide ($MAPbI_3$) is arguably the most widely explored material. Within a few years, solar cells based on $MAPbI_3$ have achieved a certified power conversion efficiency (PCE) of 22.1%.[10] Despite the exciting progress in PCE, the commercialization potency of $MAPbI_3$ based solar cells is gloomy, mainly due to the phase change and the intrinsic instability of the $MAPbI_3$ perovskite. It is known that the $MAPbI_3$ perovskite undergoes a reversible structural change from the tetragonal to cubic phase in a temperature range between 54 °C and 57 °C. This phase transition can lower the device performance by affecting the optical,[11] electrical and dielectric properties[12] of the $MAPbI_3$ perovskite. Another important issue is that $MAPbI_3$ has poor thermal stability. It decomposes in the working temperature range of optoelectronic devices and thus leads to degradation of device performance. The low thermal conductivity of the $MAPbI_3$ perovskite (~0.5 W (m K)$^{-1}$ at room temperature)[13] further worsens the condition by limiting the heat dissipation.

To address these problems, researchers have modified $MAPbI_3$ by substituting the $CH_3NH_3^+$ (MA) group with the $CH(NH_2)_2^+$ (FA) group. The new material formamidinium lead iodide ($FAPbI_3$) gives better robustness to the overall lattice and improves the material durability due to the stronger interaction between the organic FA cation and the inorganic PbI_6 cage.[14–17] In addition to the improved stability, the FA group can reduce the perovskite bandgap from 1.55 to 1.40 eV, which is closer to the theoretical optimum bandgap (1.39 eV) for a single-junction solar cell according to the Shockley–Queisser limit and thus indicates a potentially higher PCE.[18] Experimentally, solar cells based on $FAPbI_3$ with a PCE of 20.1% have already been demonstrated to prove them as promising candidates for future high-efficiency and reliable optoelectronic devices.[19] Regardless of the promising potency, the phase instability of $FAPbI_3$ poses a bottleneck challenge for practical applications. It suffers from a spontaneous α-to-δ

[a]*Department of Electronic and Computer Engineering, The Hong Kong University of Science and Technology, Clear Water Bay, Kowloon, Hong Kong SAR, China. E-mail: eezfan@ust.hk*
[b]*Department of Materials Science, Fudan University, Shanghai 200433, China*
†Electronic supplementary information (ESI) available: Fig. S1–S11 and Table 1. See DOI: 10.1039/c8nr03058h
‡These authors contributed equally to this work.

phase change at room temperature due to the larger size and the asymmetric nature of FA^+ groups (MA^+ = 216 pm, FA^+ = 253 pm).[20] In a high temperature region (>130 °C), the dynamic motion of FA^+ cations ensures that it has an isotropic orientation, which helps to stabilize the symmetry of the desired cubic structure. However, in the low temperature region (<130 °C), the FA^+ group acquires strong preferential orientations, provides strains to a specific direction and thus distorts the cubic structure into the unwanted hexagonal phase with a bandgap of 2.48 eV.[20,21] Particularly, this process is thermodynamically spontaneous regardless of the environment and it can be greatly accelerated by environmental conditions such as humidity.[14,22] To resolve this problem, numerous efforts have been exerted to maintain the black alpha phase. Alloying with other elements is a conventional approach. Smaller ions such as Cs^+,[23] MA^+ (ref. 24) and Br^- (ref. 17 and 20) have been alloyed into $FAPbI_3$ to release the strains and thus to maintain the cubic structure. Optimized Cs^+ alloyed $FAPbI_3$ ($FA_{0.85}Cs_{0.15}PbI_3$) can hold the black phase for 30 days under ambient conditions.[24] However, this alloying increases the bandgap of $FAPbI_3$ and this has partially compromised the advantage of broader light absorption of $FAPbI_3$ compared to $MAPbI_3$. More importantly, 30 days' lifetime of the black phase is still far from sufficient. Jin *et al.* stabilized the metastable black phase of the $FAPbI_3$ film *via* surface functionalization for 4 months at room temperature.[25] Long-chain alkyl or aromatic ammonium cations were used to reduce the surface energy and thus to stabilize the perovskite phase. However, this method is relatively complex as too much modification can change the morphology of $FAPbI_3$ from a smooth film into undesired nanostructures such as nanowires (NWs) and nanoplates.

Herein, we report a novel strategy to stabilize the cubic black phase of $FAPbI_3$ by using nanoengineering templates. High-density single crystalline $FAPbI_3$ NW arrays with a cubic black phase were grown inside an AAM *via* a chemical vapor deposition (CVD) method. Without further treatment, the black phase can be held over 210 days under ambient conditions. Even in an extreme environment with a Relative Humidity (RH) of 97%, the black phase can be maintained for over 8 days without phase change. We further demonstrated that their optoelectronic properties can also be maintained by assembling them into photodetectors, which can stably work over 60 days. We attributed this excellent phase stability to the spatial confinement inside the nanochannels in an AAM, which restricts the expansion of NWs in the *ab* plane that is required in α-to-δ phase transition, and the excellent passivation against water molecule invasion. This rationale was further confirmed by the observation of the α-to-δ phase transition of NWs extracted from the AAM. In this case, the NWs lost the spatial confinement and quickly turned into an undesired delta phase. Overall, here, we report a facile and effective way to address the phase instability issue of $FAPbI_3$ perovskites using a nanoengineering approach. Combining the unique geometrical tunability and high integration density inside AAMs, the three-dimensional $FAPbI_3$ NW array can be further explored for solar cells and LEDs and integrated optoelectronic applications. The insight obtained regarding the phase change can also benefit research on other perovskite materials, such as $FASnI_3$, $CsSnI_3$, *etc.*

Results and discussion

Fig. 1a schematically shows the overall growth process of $FAPbI_3$ NWs. It starts with AAM template fabrication and the details can be found in the Experimental section. The geometry of the templates, *i.e.*, the channel length, diameter and inter-pore distance, can be well controlled by the anodization and acid etching parameters. Pb nanoclusters are then electrochemically deposited at the bottom of the AAM as one precursor. This template, together with FAI powders as another precursor, is put into a 1-inch tube furnace (OTF 1200X-II, MTI) for NW growth. In this process, argon is used as a protecting gas to maintain an inert environment inside the furnace. After heating, the FAI vapor is transported to the AAM template and diffused into AAM channels. Then it reacts with Pb at the bottom and forms $FAPbI_3$ NWs. Two small bottles with a diameter of 2 cm are used to trap the FAI vapor and increase its utilization efficiency. The growth temperature is controlled between 180 °C and 240 °C and the growth time ranges from 4 h to 12 h depending on the temperature. Fig. 1b1–b3 schematically show the evolving process from Pb nanoclusters to $FAPbI_3$ NWs.

Fig. 2a1–a3 show the cross-sectional SEM images of NW growth at different stages including Pb clusters before growth (Fig. 2a1), half-grown NWs (Fig. 2a2) and over-grown NWs (Fig. 2a3). Note that the Pb clusters are only located at the bottom of AAM subchannels, and it is a natural outcome of the electrochemical deposition process.[26] Our previous reports have demonstrated that the NW growth process follows a two-step reaction: the intermediate of PbI_2 is first grown by the reaction of Pb and FAI vapor, which is then converted to

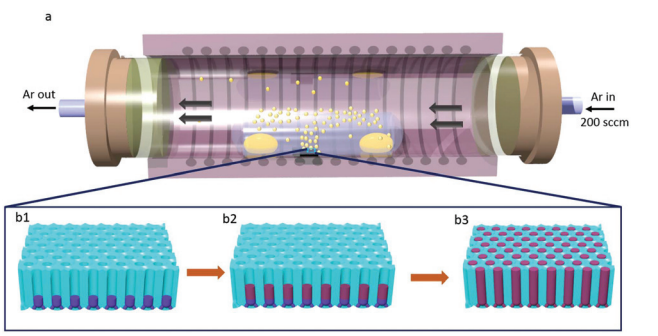

Fig. 1 (a) Overall growth schematic of $FAPbI_3$ NWs by the CVD method. (b) Schematic of the AAM template assisted growth of a vertically aligned, high density $FAPbI_3$ NW array. (b1) Pb in the AAM before NW growth. (b2) Partial $FAPbI_3$ NW growth in freestanding AAM. (b3) Completed $FAPbI_3$ NW growth in the AAM.

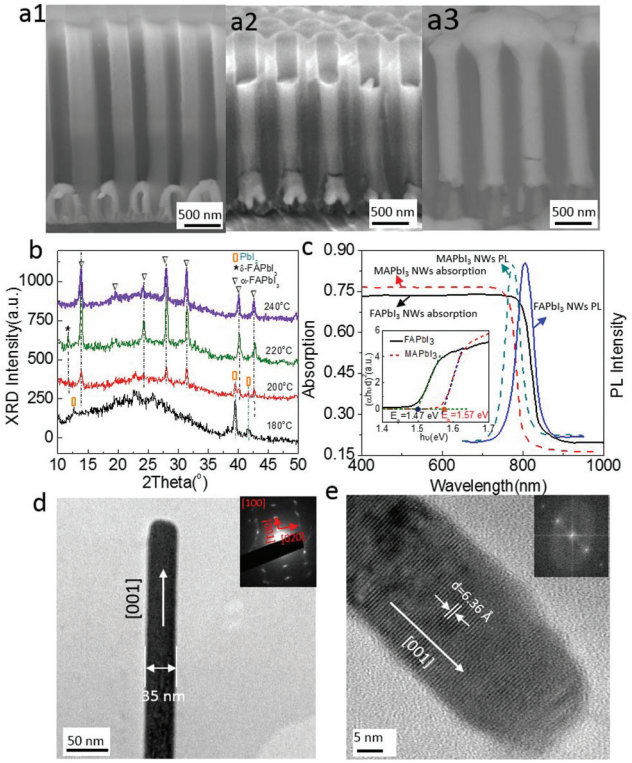

Fig. 2 (a) Cross-sectional view of SEM images of NWs grown at different stages. (a1) Lead clusters before NW growth. (a2) Half-filled NWs in growth. (a3) Fully filled NWs after complete growth. (b) XRD of $FAPbI_3$ NWs in the freestanding AAM grown at different temperatures. (c) PL and UV-Vis of $FAPbI_3$ NWs (solid line) and $MAPbI_3$ NWs (dash line) in the freestanding AAM. Inset: the calculated tauc plot of $FAPbI_3$ NWs (solid line) and $MAPbI_3$ NWs (dash line) in the freestanding AAM. (d) Low resolution TEM analysis of an individual $FAPbI_3$ NW released from the AAM. The inset is the corresponding SAED pattern. (e) High resolution TEM analysis of an individual $FAPbI_3$ NW released from the AAM channels. The inset shows the pattern after Fast Fourier transformation.

$FAPbI_3$ NWs by further reaction with the FAI vapor. The overall reaction can be expressed as:[26–28]

$$3CH(NH_2)_2I + Pb \rightarrow CH(NH_2)_2PbI_3 + 2CH_3NH_2 + N_2$$

Following this two-step growth process, the NWs grow longer and longer over time. As shown in Fig. 2a2 and a3, the NWs are tightly embedded in the AAM, indicating a well-controlled NW diameter. Fig. S1† shows the tilted angle view SEM image of NWs with slight overgrowth on the top. Clearly, we can see individual NWs with a slightly expanded diameter (~400 nm) compared to the NWs inside the channels (~230 nm). It is known that Pb has a face centered cubic crystal structure with a lattice constant of 0.495 nm. From Pb to alpha phase $FAPbI_3$ (α-$FAPbI_3$), the volume expansion can be calculated as 8.48 times. Therefore, the obtained final NW length can be pre-determined by the AAM channel diameters and the amount of Pb deposited. Although the amount of Pb can be determined from the electrochemical deposition current density and time, it is still difficult to precisely control NW growth to stop right at the top surface of an AAM which means that all NWs have identical lengths. This is an important feature for any integrated device application. Therefore, in our experiments, the NWs are always over-grown. Then NW arrays in AAMs undergo an argon ion milling process to remove the extra material on top of AAMs.

As mentioned above, the geometry of the obtained $FAPbI_3$ NWs is determined by the design of AAMs which can be tuned in a wide range by the fabrication parameters. Through this approach, geometry controllable growth of $FAPbI_3$ NW arrays can be realized. Previous research has demonstrated that geometry is another key factor affecting the properties of nanostructures in addition to the material itself. Geometry optimized nanostructures/nanomaterials exhibit unique advantages over their thin film counterpart such as improved anti-reflection and broadband absorption, enhanced ion diffusion and carrier collection efficiency as well as improved self-cleaning capability.[29–31] These advantages enabled high-performance electronic/optoelectronic devices such as high-PCE solar cells[32,33] and photodetectors with high responsivity and broadband omnidirectional light detection.[34–37] Note that these research studies mainly focused on inorganic materials such as CdS,[32] Nb_2O_5,[34] III–V group semiconductors,[36,37] *etc*. Perovskites such as $MAPbI_3$ and $FAPbI_3$ have superior material properties over these traditional materials and, therefore, geometry optimized perovskite NW arrays are expected to have high potential in future electronic/optoelectronic devices as long as their stability issues are well addressed.

Since temperature is an important parameter for CVD growth and the bulk $FAPbI_3$ material undergoes a phase transformation at an elevated temperature, we explored the growth of $FAPbI_3$ NWs at different temperatures ranging from 180 °C to 240 °C. It was discovered that this is the full temperature window for $FAPbI_3$ NW growth. Below 180 °C, FAI powders are difficult to vaporize; however, above 240 °C, they are carbonized. X-ray diffraction (XRD) and ultraviolet visible spectrum (UV-Vis) were used to characterize the structural and optical property changes of the obtained NWs, as shown in Fig. 2b and ESI Fig. S2,† respectively. The sample grown at 180 °C showed only one absorption edge at 510 nm in UV-Vis and its composition was further confirmed as PbI_2 by XRD. When the temperature increased to 200 °C, another absorption edge at 810 nm appeared. This absorption edge matches well with that of α-$FAPbI_3$ NWs. In the XRD patterns, the intensity of PbI_2 peaks is reduced while both alpha phase and delta phase $FAPbI_3$ peaks appear. These results indicate that some PbI_2 has been converted to alpha and delta phase perovskites but the sample is still a mixture of PbI_2 and the two-phase perovskite while for the sample grown at 220 °C, the PbI_2 XRD peaks completely disappeared. In the meantime, absorption at 510 nm is decreased and the absorption at 810 nm is increased. In this scenario, we attribute the absorption at 510 nm to delta phase $FAPbI_3$ (δ-$FAPbI_3$) since PbI_2 no longer exists. The increase of 810 nm absorption suggests the increase of the composition of α-$FAPbI_3$. Eventually, for the sample grown at 240 °C, there is only one absorption edge at 810 nm in UV-Vis and all the peaks

in XRD can be indexed to α-$FAPbI_3$, indicating that the grown NWs are the pure α-$FAPbI_3$ perovskite.

Fig. 2c shows the UV-Vis and photoluminescence (PL) spectra of $FAPbI_3$ NWs grown at 240 °C and $MAPbI_3$ NWs. The SEM images in Fig. S3† show the good quality of $MAPbI_3$ NWs grown by the same method at a lower temperature of 180 °C. The onset of the stabilized $FAPbI_3$ absorption spectrum occurs at ~820 nm, corresponding to a bandgap of 1.47 eV, thus allowing for wider light absorption than that of $MAPbI_3$ NWs. The PL spectrum of $FAPbI_3$ NWs shows a band-edge emission peak of 810 nm with a FWHM of ~50 nm, which is ~30 nm red-shifted from the PL peak of $MAPbI_3$ NWs. In addition to broader light absorption, $FAPbI_3$ NWs also showed much better thermal stability than $MAPbI_3$ NWs, as shown by the thermal gravimetric analysis (TGA) results in Fig. S4a.† The corresponding 1st derivatives of the TGA plots are presented in Fig. S4b.† The $FAPbI_3$ NWs undergo a weight loss at an onset temperature of about 240 °C and the highest weight loss rate is observed at 290.1 °C, which are much higher than that of the $MAPbI_3$ NWs at about 180 °C and 226.7 °C, respectively. This confirms that $FAPbI_3$ NWs are thermally much more stable than $MAPbI_3$ NWs. In addition, compared with the $FAPbI_3$ film, the temperature for the highest weight loss rate for $FAPbI_3$ NWs is about 15 °C higher. This clearly shows the effectiveness of the alumina template passivation of NWs. Overall, the much enhanced thermal stability is extremely attractive for device applications. It ensures the durability of optoelectronic devices in a harsh environment, which is a major obstacle for the applications of perovskite materials.

To further reveal the crystal structure of the obtained NWs, transmission electron microscopy (TEM) was carried out on an individual NW extracted from AAMs (Experimental section). Note that to facilitate TEM characterization, thinner NWs were prepared under the same growth conditions. Fig. 2d and e show TEM images and the selective area electron diffraction (SAED) pattern of one representative NW. As observed, the NW has a diameter of 35 nm. The clear dots in the SAED pattern indicate the single crystallinity of the observed NW. The calculated distance between two planes is 0.642 nm, which is close to the interplanar spacing measured from the high-resolution TEM (HRTEM) image in Fig. 2e (0.636 nm). This distance corresponds to the distance between two neighboring (001) planes of cubic α-$FAPbI_3$ NW.[38] These planes have grown along the axial direction and therefore result in a preferential orientation of [001]. These consistent results have further confirmed the cubic structure of the obtained NWs. In fact, this cubic structure can also be observed for many NWs that have just grown out of the AAM channel, as shown in ESI Fig. S1.†

As mentioned in the beginning, the cubic alpha phase of $FAPbI_3$ is thermodynamically unstable and it can transform to the hexagonal delta phase at room temperature regardless of the environment. Compared to the α-perovskite, δ-$FAPbI_3$ has relatively poor optoelectronic properties such as larger band gap and lower mobility and conductivity and thus is less favorable in many optoelectronic devices.[39] This α-to-δ phase transition occurs at a much faster rate than the chemical degradation of the $FAPbI_3$ perovskite material and it can dramatically change the properties of $FAPbI_3$; thus it is considered the main obstacle for the practical applications of $FAPbI_3$ perovskites. For instance, Yang *et al.* observed that the color of $FAPbI_3$ single crystals changed from black to yellow after 10 days even if they were stored under vacuum or an inert gas.[39] Many other reports have also proved the fact that α-$FAPbI_3$ can only be stored under ambient conditions for days.[14,20] Different from $MAPbI_3$, which suffers from the problem of fast decomposition, maintaining a stable cubic structure is the primary challenge for the $FAPbI_3$ perovskite.

In this study, we particularly investigated the phase stability of $FAPbI_3$ NWs. Systematic characterization including XRD, TEM and SEM were carried out to track this phase change. Specifically, after growth, a $FAPbI_3$ NW/AAM sample was stored in a regular desiccator with a relative humidity (RH) fluctuating between 18% and 40% at a temperature of 23 °C. Fig. 3a shows XRD patterns acquired from the sample around every 15 days over a period of 210 days. The XRD at Day **1** shows that after growth, all the peaks can be indexed to cubic α-$FAPbI_3$, indicating an as-grown pure alpha phase. Surprisingly, even after 210 days, there is no obvious change in the XRD pattern.

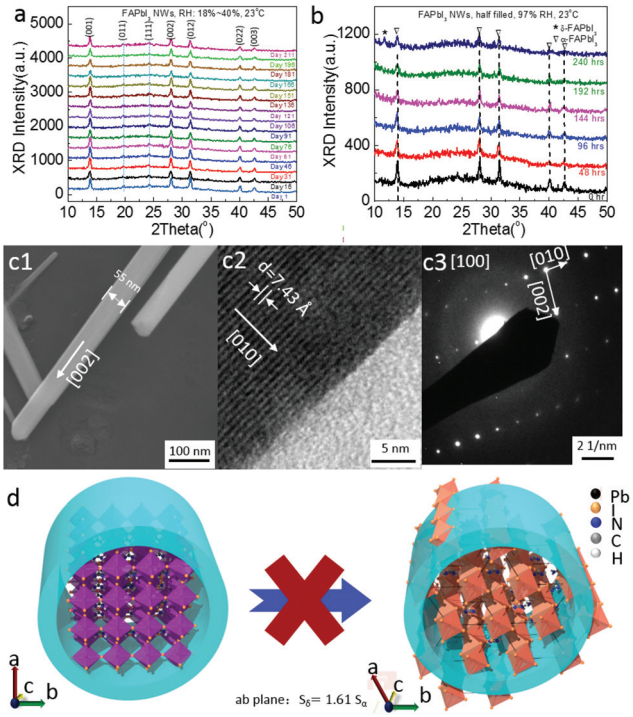

Fig. 3 (a) XRD of $FAPbI_3$ NWs in the freestanding AAM stored under ambient conditions (temperature: 23 °C, relative humidity: 18%–40%) *vs.* time. (b) XRD of $FAPbI_3$ NWs in the freestanding AAM stored under wet conditions (temperature: 23 °C, relative humidity: 97%) *vs.* time. (c) TEM analysis of an individual $FAPbI_3$ NW that is released from AAM channels and stored in a wet environment for 20 h. (c1) Low resolution TEM image of the individual NW. (b) High resolution TEM of the individual NW. (c3) SAED pattern of the individual NW. (d) Schematic of the mechanism of the AAM prohibiting the α-to-δ phase transition of $FAPbI_3$ NWs through spatial confinement.

No peaks appeared for either PbI_2 or δ-$FAPbI_3$. This result clearly indicates that the cubic phase $FAPbI_3$ NWs did not undergo decomposition and the phase change process in the period of 210 days under the given conditions. The slight drop in the XRD peak intensity can be attributed to the moisture invasion in air, which reacts with perovskites to form hydrates such as $FAPbI_3{\cdot}H_2O$ and $FA_4PbI_6{\cdot}2H_2O$.[40] Fig. S5† shows the photographs of the sample from 1st to 195th day. The consistent black color of the sample from the beginning to the end of the test period has further confirmed the excellent phase and composition stability. For comparison, we also prepared an $FAPbI_3$ film by evaporation (Experimental section). The SEM in Fig. S6† shows that the film was about ~600 nm thick with an average grain size of ~1 μm. Stored in the same environment as $FAPbI_3$ NWs, the film turned brown after 3 days and yellow after 10 days. Correspondingly, the XRD result changed from the alpha phase dominated to the delta phase dominated case. Interestingly, after heating at 150 °C for 5 min, the sample became black again. This indicates that the above process is reversible and it is the phase change rather than decomposition. Fig. S7† shows the XRD and photographs of the sample in the whole transition process. By comparing the results of $FAPbI_3$ NWs and thin film, we can conclude that $FAPbI_3$ NWs embedded in AAMs have greatly enhanced phase stability compared to $FAPbI_3$ films. Meanwhile, the material composition stability is also well maintained since there is no obvious XRD peak intensity degradation after being stored for 210 days under ambient conditions. In fact, our NWs also show better phase stability than large-size single crystal perovskites,[39] which usually exhibit better stability as their grainboundary-free nature can reduce the attack by environmental factors such as water and oxygen. In addition, our NWs are also more stable than the optimized $FAPbI_3$ films such as element alloyed samples.[23] A comparison of these samples with ours in terms of phase stability is summarized in Table 1,† which has clearly shown the alpha phase stability improvement of our sample.

Previous research has demonstrated that moisture in air can accelerate the phase transition from α-$FAPbI_3$ to δ-$FAPbI_3$ at room temperature. Priya *et al.* have observed a fast α-to-δ phase transition in 5 min after being kept in an environment with a RH of 50%, while in a dry environment with RH ~ 20%, this time would be more than hours.[20] To achieve a full understanding of the phase stability of our sample, we kept it in an extreme environment with a RH of 97%, which is created by a saturated K_2SO_4 solution as reported.[41,42] The time dependent XRD pattern and photographs were used to trace the phase change and the result demonstrated that the cubic structure of $FAPbI_3$ NWs can be held for over 192 h. This time is quite long and comparable to the time that α-$FAPbI_3$ single crystals are kept under an inert gas.[39]

In all, the cubic α-$FAPbI_3$ NWs embedded in an AAM can be retained for more than 210 days under ambient conditions with a RH of 18%–40% and 192 h at a RH of 97%. To the best of our knowledge, this is the longest time for which the cubic alpha phase can be maintained both under ambient and wet conditions. Note that, currently, there is still no sign of phase change for the NW sample measured after 210 days; therefore, the actual life time of α-$FAPbI_3$ can be much longer. Our results have proved that the AAM is an effective tool to help the $FAPbI_3$ perovskite to overcome its phase instability issue.

The form of NWs is reported to be helpful in stabilizing the cubic phase of the perovskite material due to the high surface energy introduced by their large surface/volume ratio.[43] To reveal whether the enhanced phase stability in our $FAPbI_3$ NWs is the intrinsic NW property or the effect of AAM passivation, we performed a control experiment to observe whether individual freestanding NWs can undergo phase change or not. In this experiment, the NWs were extracted from AAMs by grinding and sonication in chlorobenzene. The NW/chlorobenzene suspensions were dropped on a TEM grid and dried for TEM characterization. To exclude the effect of the solvent, $FAPbI_3$ films were made to go through the same process for comparison. Fig. S8† shows the UV-Vis spectra of the $FAPbI_3$ film at different time stages, in which there is no obvious band edge shift after sonication in chlorobenzene. This indicates that chlorobenzene does not trigger the phase change and the decomposition of α-$FAPbI_3$. Any changes in the NWs are caused by the loss of AAM confinement and all changes can be identified by TEM observation. As shown in Fig. 3b, NWs in AAMs did not show any sign of phase change even after being kept at a RH of 97% for 192 h. Therefore, we kept the TEM grid with cubic phase NWs at a RH of 97% for comparison. The results show that these freestanding NWs have undergone α-to-δ phase transition after 20 h storing at a RH of 97%. Specifically, the HRTEM image in Fig. 3c2 shows that a representative NW has an interplanar spacing of 0.747 nm along the radial direction that corresponds to the distance between two neighbouring (010) planes of the hexagonal $FAPbI_3$ NW.[39,44] The SAED in Fig. 3c3 shows two interlayer spacings of 0.743 nm and 0.396 nm. The first one is consistent with that from HRTEM, corresponding to the (010) planes of the hexagonal $FAPbI_3$ NW along the radial direction. The second one, which is perpendicular to the radial direction, namely the NW axial direction, matched well with the distance of the neighbouring (002) planes.[45] This result indicates that once a NW becomes free standing, it is prone to phase change from the cubic alpha phase to the hexagonal delta phase. Meanwhile, it is intriguing that as shown in Fig. S9b,† even when the NWs in the AAM were undergoing decomposition, the material still remained in the cubic phase. To explain this observation, we considered the lattice constant change and the *ab* lattice plane area change. According to the results shown above, both cubic phase NWs in AAMs and hexagonal phase free standing NWs have an axial direction of [001]. Thus *ab* planes are perpendicular to the NW axial direction as well as AAM nanochannel axial direction. For the cubic phase, $a = b = c = 0.636$ nm and for the hexagonal phase, $a = b = 0.866$ nm and $c = 0.795$ nm.[45] Therefore, after the phase change, the area of the *ab* plane is around 1.61 times that before the phase change. This *ab* plane expansion in fact has been observed by TEM which shows an increase of the NW diameter after the phase change, as seen in Fig. 2f and 3c1. For a free standing

NW, such *ab* plane expansion is allowed, and therefore, phase transformation can happen. However for NWs in an AAM, the *ab* plane expansion is prohibited due to the spatial confinement in the *ab* direction inside the nanochannels. Therefore, NW α-to-δ phase transition is inhibited in AAMs. The mechanism described above is schematically shown in Fig. 3d. In our work, we have used high humidity to accelerate the phase change of the free standing NWs. However, AAMs can also provide excellent protection against water molecule invasion on perovskite NWs.[27,46] Therefore, we attribute the excellent cubic phase stability to a combinational effect of inhibiting *ab* lattice plane expansion and effective blockage of the diffusion of water and oxygen molecules within the templates. Fig. S10† shows the phase stability testing result of large diameter $FAPbI_3$ NWs (diameter: ~450) embedded in the AAM. After 5 days at a RH of 97%, the peaks corresponding to δ-$FAPbI_3$ appear, indicating poorer phase stability compared to smaller diameter $FAPbI_3$ NWs. The diameter dependent phase stability is due to the weaker passivation and spatial confinement of large-diameter AAM nanochannels.

Fig. S11† shows the UV-Vis and PL measurements of the sample on the 1st and 210th day of storage under ambient conditions. The overlap of these curves indicates that their optical properties can also be well maintained for at least 210 days. The stable structural and optical properties indicate the promising potency of our $FAPbI_3$ NWs for reliable optoelectronic devices. In our work, we have fabricated and characterized NW array photodetectors. Fig. 4a schematically shows the configuration of a device. In this configuration, the Al substrate serves as the bottom electrode of the device and a layer of ITO with a thickness of 100 nm was sputtered on top of NWs serving as the top electrode. One unique advantage of the NW array is that it has a ultra-high density. In the current work, the NWs are hexagonally arranged with a pitch of 500 nm and the density can be calculated as 4×10^8 cm^{-2}. Considering that the individual photodetector has an area of ~7.06 mm^2, there are 2.8×10^7 NWs in each device. In the future, the device footprint can be scaled down to a few hundred nanometer level since individual NWs are well isolated. This can be used for ultra-high resolution imaging applications.[26]

Fig. 4b shows the current–voltage characteristics (*I*–*V*) of a photodetector illuminated with an increasing intensity of a halogen light source. The asymmetric nature of the *I*–*V* curves suggests that the device is a typical Schottky photodiode. This can be explained by the asymmetric contact material on top and bottom of the NW array and the resulting band bending at the contact interface is shown in the inset of Fig. 4b. Clearly, the device is sensitive to light and the current increases with the increase of the light intensity. To further characterize the photoresponse, the device was measured with chopped optical input from a 450 nm laser with three different intensities. Fig. 4c shows the *I*–*t* sampling plot of a photodetector under a fixed bias of 7 V. The stable and repeatable dark and light currents in all the four cycles indicate the excellent device reliability and reproducibility. The sharp change in the current

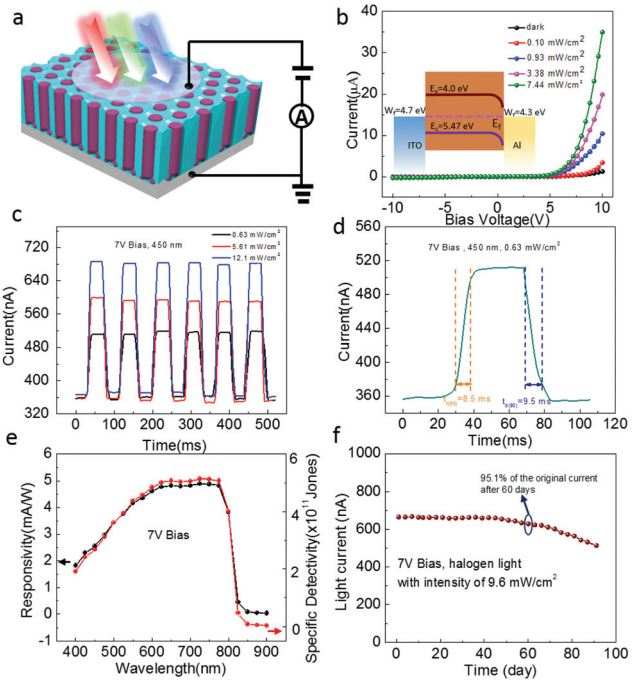

Fig. 4 (a) Schematic of the configuration of a photodetector based on $FAPbI_3$ NWs embedded in the AAM. (b) *I*–*V* curves of a photodetector under different illumination intensities (white halogen light). Inset: band structure of a photodetector under zero bias and dark conditions. (c) *I*–*t* curves of a photodetector under exposure to different illumination intensities (450 nm light). (d) Response time analysis under light of 0.63 mW cm^{-2} under +7 V bias voltage. (e) Responsivity measurement under +7 V bias voltage. (f) Light current decay of a photodetector under a bias of +7 V and illumination of 9.6 mA cm^{-2}, using halogen light.

with light ON and OFF indicates a high photoresponse speed. Fig. 4d further shows the photocurrent rise time and fall time, which are defined as t_{90}, that is the time needed to achieve 90 percent of the current change. Thus the rise and fall time were found to be 8.5 ms and 9.5 ms, respectively. This response time is shorter than that of many perovskite based photodetectors probably due to the good crystallinity of NWs that can increase the charge transportation velocity.[47,48] Further improvement of the response speed can be conceivably achieved by reducing the NW length to reduce charge carrier transit time and NW resistance, and shrinking the pixel size to reduce the capacitance between the top and bottom electrodes in the future. In addition to the response time, responsivity and specific detectivity are also important figures-of-merit to quantify the performance of a photodetector. Fig. 4e shows the measured responsivity and detectivity under a bias of 7 V. Clearly, the responsivity gradually increases from 1.8 mA W^{-1} to 4.7 mA W^{-1} as the wavelength increases from 400 to 600 nm, gets stabilized at ~5 mA W^{-1} in the range of 600 nm–800 nm and demonstrates a sudden drop at 800 nm. The relatively low responsivity in the range of 400–600 nm is due to the short penetration depth of the short-wavelength light, which has a prolonged hole transportation path to elec-

trodes and thus reduced the hole collection efficiency. The sudden drop at 800 nm indicates absorption cuts off at around 800 nm. This is consistent with the optical measurement result and has further confirmed the cubic nature of our $FAPbI_3$ NWs. The calculated specific detectivity is 2×10^{11}–5×10^{11} Jones. Fig. 4f shows a plot of current under radiation of 9.6 mW cm^{-2} *vs.* time. To test the device stability, the photodetector was stored in the same environment as that of the pristine $FAPbI_3$ NWs and was taken out for measurement every 3 days. It is clearly seen that after 60 days, the light current maintains 95.1 percent of its original value. This indicates that the photodetector can steadily work for over 60 days without obvious degradation. The device stability shown here indicates that our NWs are promising building blocks for stable and reliable optoelectronic devices. Note that the bias voltage of 7 V here is higher than that of many photodetectors.[47,48] As the electric field can induce degradation into perovskite materials by causing ion migration,[49,50] and this process can be accelerated by the existence of light, the device stability can be further improved by reducing the bias voltage and light intensity.

Conclusions

In summary, here, we demonstrated a CVD process to grow formamidinium lead iodide perovskite NWs inside AAM templates. The structural characterization showed that NWs are single crystalline with a cubic phase at room temperature. Without further treatment, this cubic phase, which is desirable for most optoelectronic devices, can be held for quite a long time both under dry and wet conditions. This intriguing fact is attributed to the spatial confinement provided by AAM nanochannels, which prohibits the unwanted α-to-δ phase transition by restricting the expansion of NWs in the *ab* plane, and the excellent passivation against the invasion of water molecules. To demonstrate the device applications, these vertical NWs were configured as photodetectors demonstrating reasonable performance. Overall, the discovery reported here suggests a facile and effective way to address the phase instability issue of $FAPbI_3$ perovskites and provides an additional impetus to explore the application of $FAPbI_3$ in practical optoelectronic devices.

Experimental

AAM fabrication

The AAM fabrication follows the conventional two-step anodization of high-purity aluminum foils reported previously. In brief, pure aluminum (Al) foil with a thickness of 0.25 mm was cleaned by sonication in acetone and rinsed with isopropyl alcohol and water. After drying, the sheets were electrochemically polished in an acidic solution (25 vol% $HClO_4$ mixed with 75 vol% absolute CH_3CH_2OH) for 2 min under 12 V at 10 °C. After polishing, the chips were immersed in a weak acid solution (deionized water : ethylene glycol : H_3PO_4 = 200 : 100 : 1, by volume) for anodization under a 200 V d.c. bias, at 10 °C for 10 h. Afterwards, the first anodization layer was etched away in a mixture of phosphoric acid (6 wt% H_3PO_4 and 1.8 wt% CrO_3) at 98 °C for 50 min. This is followed by the second anodization which was carried out under the same conditions for 40 min to obtain an approximately 2 μm-thick AAM. Finally, the template was further etched in a H_3PO_4 aqueous solution (5 wt%, 52 °C) for 10 min to widen the channel diameter to 230 nm.

For the well-ordered AAM, the Al sheets were imprinted using a silicon mold (hexagonally ordered pillar array with a height of 200 nm, a diameter of 200 nm, and a pitch of 500 nm) with a pressure of approximately 2×10^4 N cm^{-2} before first anodization. The first anodization time is reduced to 10 min, which corresponds to a shorter first etching time of 10 min. The AAM for the TEM sample undergoes anodization in a solution of 0.3 M oxalic acid under the bias voltage of 60 V. The first etching time is 3 h and the second etching step is also skipped to ensure a small pore diameter of ~30 nm.

Barrier thinning and Pb electrodeposition

Barrier thinning is a process to thin down the alumina layer at the bottom of AAM nanochannels by reducing the bias voltage. This process is in fact another anodization step carried out in a 0.2 M H_3PO_4 solution at room temperature controlled by using a computer programmed Keithley 2400. In the beginning, the Keithley 2400 was set in voltage source mode, the anodization voltage was gradually ramped up to 160 V and the electric current I_0 was recorded. Then the Keithley 2400 was switched to current source mode and the current was set to $I_0/2$. A gradual decrease of the voltage was then observed. When the voltage declining rate was slower than 3 V min^{-1}, the current was then set to $I_0/4$ so that the voltage declining process continued. When the voltage reached down to 4 V, the process was terminated.

After barrier thinning, the chip is immersed in solution (1.7 g lead(II) chloride ($PbCl_2$) and 25 g trisodium citrate ($Na_3C_6H_5O_7$) dissolved in 100 ml water) for Pb electrodeposition through a 3-electrode setup controlled by using a potentiostat (SG 300, Gamry Instruments). An alternative sinusoidal voltage with a frequency of 60 Hz was applied, and the amplitude was increased from 3.4 to 9 V to maintain a peak current density of ~2.2 mA cm^{-2} at the negative deposition cycle. After deposition, the chip was rinsed with deionized water several times to remove the adsorbed chemicals. The achieved Pb was ~200 nm thick at the bottom of the AAM.

Growth of $FAPbI_3$ NWs

The growth of $FAPbI_3$ NWs was a CVD process with Pb and FAI vapor as precursors, which was carried out in a one-inch tube furnace (OTF 1200X-II, MTI). The FAI powder was kept at the bottom of a glass bottle (diameter of 2 cm and length of 3 cm) while a AAM/Pb chip was placed near its opening end. The whole bottle was then put into the furnace with the AAM chip close to the temperature sensor of the furnace to ensure an accurate growth temperature. A second bottle with FAI

powders was used to trap the FAI vapor, which was placed in an opposite direction of the first bottle, with its opening end facing the AAM chip. An argon flow of 300 sccm was used as the protecting gas. The furnace is then heated to the desired temperature (180 °C–240 °C) in 20 min and was maintained at this temperature for several hours for NW growth. After growth, the furnace was open to ensure fast drop of the sample temperature from the growth temperature to room temperature. In addition, $MAPbI_3$ NWs were grown for comparison. It follows the same steps in the same setup but with MAI powders as a precursor. The growth temperature is controlled at 180 °C and the growth time is typically 3 h.

XRD characterization

The XRD was carried out on the equipment of X'pert Pro (PANalytical) with a Cu K-alpha line (wavelength = 0.15408 nm) as an X-ray source. For XRD characterization, free standing NWs/AAM was used to avoid the interference of the Al substrate. As the perovskite is easy to decompose in the solvent, the Al substrate is etched away before NW growth. Specifically, the Al substrate was etched away using a saturated $HgCl_2$ solution. Before that, the AAM/Al chip was first covered by a layer of crystal bond (509, Ted Pella, Inc.) to protect the electrochemically deposited Pb from being etched away. After $HgCl_2$ etching, the sample was transferred into acetone for 1 h to remove the crystal bond layer. Afterwards, the AAM was dried at 80 °C on a hotplate for 2 min and it was naturally separated from the Si substrate. These NWs grown on this free-standing AAM were then taken out for XRD characterization.

TEM characterization

TEM is carried out on the equipment of JEM 2010 (JEOL) under a bias of 200 kV. It cannot be directly performed as the NWs are tightly embedded inside the AAM channels. Conventional methods such as releasing NWs by dissolving the AAM in an acidic or alkaline solvent also do not fit for our sample as the perovskites are easy to decompose in these solvents. Herein, we invented a novel method to release the NWs from AAM channels through a method that combined grinding and sonication. In specific, the NWs were first ground into small chips in a mortar and more NWs are, therefore, exposed to air. These small chips were then transferred to solvent chlorobenzene for sonication for 20 min. This energy from sonication can peel the exposed NWs off from AAM channels. The brown suspension was then dropcast onto a copper grid and dried for TEM characterization.

Preparation of an $FAPbI_3$ film

An $FAPbI_3$ film is fabricated by an evaporation method. Specifically, PbI_2 of 150 nm thickness was thermally evaporated onto the FTO substrate at the rate of 1 Å s^{-1} which is followed by the evaporation of the FAI layer of 400 nm thickness. The whole sample was then annealed at a temperature of 150 °C in air for 40 min to form the cubic $FAPbI_3$ film.

Conflicts of interest

There are no conflicts to declare.

Acknowledgements

This work was supported by the National Natural Science Foundation of China (project 51672231) and the General Research Fund (Project No. 612113 and 16237816) from the Hong Kong Research Grant Council. The authors acknowledge the support received from the Center for 1D/2D Quantum Materials and State Key Laboratory on Advanced Displays and Optoelectronics at HKUST.

Notes and references

1 G. W. Adhyaksa, E. Johlin and E. C. Garnett, *Nano Lett.*, 2017, **17**, 5206–5212.
2 M. M. Tavakoli, Q. Lin, S. F. Leung, G. C. Lui, H. Lu, L. Li, B. Xiang and Z. Fan, *Nanoscale*, 2016, **8**, 4276–4283.
3 Y. Rong, S. Venkatesan, R. Guo, Y. Wang, J. Bao, W. Li, Z. Fan and Y. Yao, *Nanoscale*, 2016, **8**, 12892–12899.
4 Y. Mi, Z. Liu, Q. Shang, X. Niu, J. Shi, S. Zhang, Q. Zhang, T. Wu and X. Qiu, *Small*, 2018, **14**, 1703136.
5 Q. Zhang, R. Su, W. Du, X. Liu, L. Zhao, S. T. Ha and Q. Xiong, *Small Methods*, 2017, **1**, 1700163.
6 N. Wang, L. Cheng, R. Ge, S. Zhang, Y. Miao, W. Zou and Y. Wei, *Nat. Photonics*, 2016, **10**, 699.
7 C. M. Sutter-Fella, Y. Li, M. Amani, J. W. Ager III, F. M. Toma, E. Yablonovitch and A. Javey, *Nano Lett.*, 2015, **16**, 800–806.
8 W. Deng, L. Huang, X. Xu, X. Zhang, X. Jin, S. T. Lee and J. Jie, *Nano Lett.*, 2017, **17**, 2482–2489.
9 M. He, Y. Chen, H. Liu, J. Wang, X. Fang and Z. Liang, *Chem. Commun.*, 2015, **51**, 9659–9661.
10 National Renewable Energy Laboratory (NREL) Efficiency Chart, http://www.nrel.gov/ncpv/images/efficiency_chart.jpg (accessed on 28th May 2017).
11 T. Baikie, Y. Fang, J. M. Kadro, M. Schreyer, F. Wei, S. G. Mhaisalkar and T. J. White, *J. Mater. Chem. A*, 2013, **1**, 5628–5641.
12 M. N. F. Hoque, M. Yang, Z. Li, N. Islam, X. Pan, K. Zhu and Z. Fan, *ACS Energy Lett.*, 2016, **1**, 142–149.
13 R. Heiderhoff, T. Haeger, N. Pourdavoud, T. Hu, M. Al-Khafaji, A. Mayer and T. Riedl, *J. Phys. Chem. C*, 2017, **121**, 28306–28311.
14 E. Smecca, Y. Numata, I. Deretzis, G. Pellegrino, S. Boninelli, T. Miyasaka and A. Alberti, *Phys. Chem. Chem. Phys.*, 2016, **18**, 13413–13422.
15 T. M. Koh, K. Fu, Y. Fang, S. Chen, T. C. Sum, N. Mathews and T. Baikie, *J. Phys. Chem. C*, 2014, **118**, 16458–16462.
16 S. Pang, H. Hu, J. Zhang, S. Lv, Y. Yu, F. Wei and G. Cui, *Chem. Mater.*, 2014, **26**, 1485–1491.
17 G. E. Eperon, S. D. Stranks, C. Menelaou, M. B. Johnston, L. M. Herz and H. J. Snaith, *Energy Environ. Sci.*, 2014, **7**, 982–988.

18 S. Rühle, *Sol. Energy*, 2016, **130**, 139–147.
19 W. S. Yang, J. H. Noh, N. J. Jeon, Y. C. Kim, S. Ryu, J. Seo and S. I. Seok, *Science*, 2015, **348**, 1234–1237.
20 X. Zheng, C. Wu, S. K. Jha, Z. Li, K. Zhu and S. Priya, *ACS Energy Lett.*, 2016, **1**, 1014–1020.
21 T. Chen, B. J. Foley;, C. Park, C. M. Brown, L. W. Harriger, J. Lee and S. H. Lee, *Sci. Adv.*, 2016, **2**, e1601650.
22 S. Wozny, M. Yang, A. M. Nardes, C. C. Mercado, S. Ferrere, M. O. Reese and K. Zhu, *Chem. Mater.*, 2015, **27**, 4814–4820.
23 Z. Li, M. Yang, J. S. Park, S. H. Wei, J. J. Berry and K. Zhu, *Chem. Mater.*, 2015, **28**, 284–292.
24 Y. Zhang, G. Grancini, Y. Feng, A. M. Asiri and M. K. Nazeeruddin, *ACS Energy Lett.*, 2017, **2**, 802–806.
25 Y. Fu, T. Wu, J. Wang, J. Zhai, M. J. Shearer, Y. Zhao and S. Jin, *Nano Lett.*, 2017, **17**, 4405–4414.
26 L. Gu, M. M. Tavakoli, D. Zhang, Q. Zhang, A. Waleed, Y. Xiao and Z. Fan, *Adv. Mater.*, 2016, **28**, 9713–9721.
27 A. Waleed, M. M. Tavakoli, L. Gu, Z. Wang, D. Zhang, A. Manikandan and Z. Fan, *Nano Lett.*, 2016, **17**, 523–530.
28 M. M. Tavakoli, A. Waleed, L. Gu, D. Zhang, R. Tavakoli, B. Lei and Z. Fan, *Nanoscale*, 2017, **9**, 5828–5834.
29 M. Yu, Y. Z. Long, B. Sun and Z. Fan, *Nanoscale*, 2012, **4**, 2783–2796.
30 J. Lee, B. Hua, S. Park, M. Ha, Y. Lee, Z. Fan and H. Ko, *Nanoscale*, 2014, **6**, 616–623.
31 Z. Fan, D. J. Ruebusch, A. A. Rathore, R. Kapadia, O. Ergen, P. W. Leu and A. Javey, *Nano Res.*, 2009, **2**, 829–843.
32 Z. Fan, H. Razavi, J. W. Do, A. Moriwaki, O. Ergen, Y. L. Chueh, P. W. Leu, J. C. Ho, T. Takahashi, L. A. Reichertz and A. Javey, *Nat. Mater.*, 2009, **8**, 648–653.
33 X. Zheng, Z. Wei, H. Chen, Q. Zhang, H. He, S. Xiao, Z. Fan, K. S. Wong and S. Yang, *Nanoscale*, 2016, **8**, 6393–6402.
34 X. S. Fang, L. F. Hu, K. F. Huo, B. Gao, L. J. Zhao, M. Y. Liao, P. K. Chu, Y. Bando and D. Golberg, *Adv. Funct. Mater.*, 2011, **21**, 3907–3915.
35 F. Teng, L. X. Zheng, K. Hu, H. Y. Chen, Y. M. Li, Z. M. Zhang and X. S. Fang, *J. Mater. Chem. C*, 2016, **4**, 8416–8421.
36 D. Zheng, J. Wang, W. Hu, L. Liao, H. Fang, N. Guo, P. Wang, F. Gong, X. Wang, Z. Fan and X. Wu, *Nano Lett.*, 2016, **16**, 2548–2555.
37 H. Wang, H. Zhen, S. Li, Y. Jing, G. Huang, Y. Mei and W. Lu, *Sci. Adv.*, 2016, **2**, p.e1600027.
38 L. Q. Xie, L. Chen, Z. A. Nan, H. X. Lin, T. Wang, D. P. Zhan and Z. Q. Tian, *J. Am. Chem. Soc.*, 2017, **139**, 3320–3323.
39 Q. Han, S. H. Bae, P. Sun, Y. T. Hsieh, Y. M. Yang, Y. S. Rim and Y. Yang, *Adv. Mater.*, 2016, **28**, 2253–2258.
40 A. M. Leguy, Y. Hu, M. Campoy-Quiles, M. I. Alonso, O. J. Weber, P. Azarhoosh and P. Docampo, *Chem. Mater.*, 2015, **27**, 3397–3407.
41 L. Gu, K. Zheng, Y. Zhou, J. Li, X. Mo, G. R. Patzke and G. Chen, *Sens. Actuators, B*, 2011, **159**, 1–7.
42 F. E. M. O'brien, *J. Sci. Instrum.*, 1948, **25**, 73–76.
43 A. Swarnkar, A. R. Marshall, E. M. Sanehira, B. D. Chernomordik, D. T. Moore, J. A. Christians, T. Chakrabarti and J. M. Luther, *Science*, 2016, **354**, 92–95.
44 N. J. Jeon, J. H. Noh, W. S. Yang, Y. C. Kim, S. Ryu, J. Seo and S. I. Seok, *Nature*, 2015, **517**, 476–480.
45 C. C. Stoumpos, C. D. Malliakas and M. G. Kanatzidis, *Inorg. Chem.*, 2013, **52**, 9019–9038.
46 A. Waleed, M. M. Tavakoli, L. Gu, S. Hussain, D. Zhang, S. Poddar and Z. Fan, *Nano Lett.*, 2017, **17**, 4951–4957.
47 Y. Lee, J. Kwon, E. Hwang, C. H. Ra, W. J. Yoo, J. H. Ahn and J. H. Cho, *Adv. Mater.*, 2015, **27**, 41–46.
48 H. R. Xia, J. Li, W. T. Sun and L. M. Peng, *Chem. Commun.*, 2014, **50**, 13695–13697.
49 S. Bae, S. Kim, S. W. Lee;, K. J. Cho, S. Park, S. Lee and D. J. Kim, *J. Phys. Chem. Lett.*, 2016, **7**, 3091–3096.
50 N. Ahn, K. Kwak, M. S. Jang, H. Yoon, B. Y. Lee, J. K. Lee and M. Choi, *Nat. Commun.*, 2016, **7**, 13422.